

Fe Line Diagnostics of Cataclysmic Variables and Galactic Ridge X-ray Emission

Xiao-jie Xu

School of Astronomy and Space Science and Key Laboratory of Modern Astronomy and
Astrophysics, Nanjing University, Nanjing, P. R. China 210093

Q. Daniel Wang

Department of Astronomy, University of Massachusetts Amherst, MA 21003, U.S.A.

Xiang-Dong Li

School of Astronomy and Space Science and Key Laboratory of Modern Astronomy and
Astrophysics, Nanjing University, Nanjing, P. R. China 210093

Received _____; accepted _____

ABSTRACT

The properties of the Galactic Ridge X-ray Emission (GRXE) observed in the 2-10 keV band place fundamental constraints on various types of X-ray sources in the Milky Way. Although the primarily discrete origin of the emission is now well established, the responsible populations of these sources remain uncertain, especially at relatively low fluxes. To provide insights into this issue, we systematically characterize the Fe emission line properties of the candidate types of the sources in the solar neighborhood and compare them with those measured for the GRXE. Our source sample includes 6 symbiotic stars (SSs), 16 intermediate polars (IPs), 3 polars, 16 quiescent dwarf novae (DNe) and 4 active binaries (ABs); they are all observed with the *Suzaku* X-ray Observatory. The data of about 1/4 of these sources are analyzed for the first time. We find that the mean equivalent width ($EW_{6.7}$) of the 6.7-keV line and the mean 7.0/6.7-keV line ratio are 107 ± 16.0 eV and 0.71 ± 0.04 for intermediate polars and 221 ± 135 eV and 0.44 ± 0.14 for polars, respectively, which are all substantially different from those (490 ± 15 eV and 0.2 ± 0.08) for the GRXE. Instead, the GRXE values are better agreed by the $EW_{6.7}$ (438 ± 84.6 eV) and the ratio (0.27 ± 0.06) observed for the DNe. We further find that the $EW_{6.7}$ is strongly correlated with the 2-10-keV luminosity of the DNe, which can be characterized by the relation $EW_{6.7} = (438 \pm 95 \text{ eV})(L/10^{31} \text{ ergs s}^{-1})^{(-0.31 \pm 0.15)}$. Accounting for this correlation, the agreement can be improved further, especially when the contributions from other classes sources to the GRXE are considered, which all have low $EW_{6.7}$ values. We conclude that the GRXE mostly consists of typically faint, but numerous DNe, plus ABs, while magnetic CVs are probably mainly the high-flux representatives of the responsible populations and dominate the GRXE only in harder energy bands.

Subject headings: Galaxy: bulge — X-rays: binaries — cataclysmic variables

1. Introduction

Although discovered more than 30 years ago, the exact origin of the Galactic Ridge X-ray Emission (GRXE) observed in the 2-10 keV range remains largely uncertain (e.g., Worrall et al. 1982; Revnivtsev et al. 2009; Hong et al. 2012). The overall spectral shape of the GRXE, with a total 2-10 keV luminosity of $\sim (1 - 2) \times 10^{38} \text{ erg s}^{-1}$, can be approximately characterized as a two-temperature optically thin thermal plasma with $kT_1 \sim 1 \text{ keV}$ and $kT_2 \sim 15 \text{ keV}$ over the 2 - 50 keV (or $kT_2 \sim 6 \text{ keV}$ over 2-10 keV) range covered by the *Suzaku* (e.g., Yuasa et al. 2010, 2012). The spectrum of the GRXE also contains emission lines; the three most prominent ones are from Fe K α transitions: 6.4-keV line from neutral or weakly-ionized species, 6.7-keV and 7.0-keV lines from Helium-like and Hydrogen-like ions (e.g., Uchiyama et al. 2013). Both the line and continuum properties of the GRXE provide important clues about its origin.

Two scenarios have been proposed to explain the GRXE. The first scenario assumes that the GRXE arises primarily from truly diffuse hot plasma in and near the Galactic disk, while the second proposes that the emission represents a superposition of numerous point-like sources, including their light scattered by the interstellar medium (ISM) (Molaro et al. 2014). The 1 Ms *Chandra* deep exposure carried out by Revnivtsev et al. (2009) toward the ‘Limiting Window’ in the Galactic bulge successfully resolved out about 80% of the GRXE (at $\sim 6 \text{ keV}$) into individual sources with a detection limit down to the 2-10 keV luminosity of $\sim 10^{30} \text{ erg s}^{-1}$ at the Galactic center distance of 8 kpc (see also Hong et al. 2012). Furthermore, the spatial distribution of the GRXE closely follows that of the stellar mass in the Galaxy (Revnivtsev et al. 2006). These results strongly support the point source scenario, leaving little room for a substantial contribution from the diffuse hot plasma, probably except for the Galactic center region ($\lesssim 0.5^\circ$ from Sgr A*; e.g., Uchiyama et al. 2011).

However, the nature of the point sources responsible for the GRXE remains elusive. It has been suggested that the dominating source population might be cataclysmic variables (CVs), or more specifically, magnetic ones (mCVs), plus a minor contribution from active binaries (ABs; e.g., Revnivtsev et al. 2009). CVs are binaries, each consisting a white dwarf (WD) accreting matter from a main-sequence or red-giant companion. Based on the magnetic field strengths of the WDs, CVs are classified into magnetic [including polars and intermediate polars (IPs)] or non-magnetic ones [including novae, quiescent dwarf novae (DNe), symbiotic star (SSs), etc.]. Comparatively less luminous are ABs, binaries of normal stars whose X-ray emission is enhanced by strong magnetic field due to spin-orbital coupling. The luminosity functions (LFs) of nearby CVs and ABs were studied by Sazonov et al. (2006); Byckling et al. (2010); Pretorius & Knigge (2012). Based on their LFs, as well as spectral and temporal behaviors (Revnivtsev et al. 2009; Hong et al. 2012), relative bright point sources (with the 2-10 keV luminosity $L_X \gtrsim 10^{32} \text{ erg s}^{-1}$) observed in the GRXE are mostly considered to be mCVs. The nature of fainter sources, especially those below $10^{31} \text{ erg s}^{-1}$ is much less clear. Individually they are typically too faint to allow spectral and temporal analyses with existing X-ray data. Collectively, the LF of such sources suggests that they contribute more to the GRXE than those bright ones; the sources in the range of $L_X \sim 10^{30-31} \text{ erg s}^{-1}$, for example, are about 30 times more in numbers than the bright ones and account for 75% of the resolved emission in the 6-8 keV range (Revnivtsev et al. 2009). The LF may, however, vary significantly from the the stellar disk, to the bulge, and to the center of the Galaxy (e.g., Perez et al. 2015). So the consideration of the local LF alone cannot be conclusive with regard to the nature of the sources in the GRXE. Therefore, an improved understanding of the GRXE will be interesting not only for its own right, but for providing fundamental constraints on the integrated properties of various X-ray source populations in the Galaxy as well. These constraints are also essential to the correct estimation and subtraction of the source contributions and hence to the study of

diffuse hot plasma in other galaxies (e.g., Li & Wang 2007).

We here focus on the use of the diagnostic Fe K emission lines to probe the nature of the faint sources in the GRXE in the 2-10 keV band. To do so, we first characterize the mean intensities of the emission lines from local sources of various known classes (mCVs, DNe, ABs, SSs, and polars). Specifically, both the EW of the 6.7-keV ($EW_{6.7}$) and the flux ratio of the 7.0 to 6.7 keV lines ($I_{7.0}/I_{6.7}$) are sensitive probes of hot plasma temperature (T ; Fig. 1). $EW_{6.7}$ always decreases, while $I_{7.0}/I_{6.7}$ increases with increasing T in the 1-20 keV range. In an mCV, an accretion disk is not expected (at least near the WD); the gravitational potential energy of the infall gas (e.g., in an accretion column) is converted into the heat almost entirely at a standing shock near the surface of the WD (e.g., Longair 2011). In contrast, for a non-magnetic CV, a cool accretion disk is expected, which radiates about half of the gravitational energy and hardly contributes to the X-ray emission. The other half of the energy, retained in the Keplerian motion at the inner boundary of the disk, can effectively heat the gas when eventually falling onto the WD through the boundary layer. The maximum temperature that the gas can reach depends on the exact heating mechanism (e.g., via a single shock or a series of weaker ones), but should be about a factor of $\gtrsim 2$ smaller than that for an mCV of same WD mass. This expectation is consistent with existing observations, which show that mCVs generally have smaller $EW_{6.7}$ and greater $I_{7.0}/I_{6.7}$ than non-magnetic CVs (e.g., Ishida & Ezuka 1999; Ezuka & Ishida 1999; Anzolin et al. 2009; Mukai et al. 2009; Ishida et al. 2009). Moreover, unlike the EWs of the Fe lines, $I_{7.0}/I_{6.7}$ is independent of either the metallicity of the hot plasma or the continuum emission, which can be strongly affected by X-ray absorption and/or reflection. Thus $I_{7.0}/I_{6.7}$ provides the most reliable diagnostic of the plasma temperature in the 1-20 keV range. Interestingly, the typical temperature of GRXE falls in this range (Yuasa et al. 2012; Uchiyama et al. 2013), making Fe lines sensitive probes in comparisons among different classes of CVs (with typical temperatures below 20 keV) or with the GRXE.

Additional constraint on the plasma temperature can be obtained from the measurement of the 6.4-keV emission line, which is predominantly from the fluorescence of ionizing photons (> 7.12 keV) by cold irons. The strength of the line, relative to the other lines or to the continuum, is sensitive to both the temperature of the hot plasma, which produces the photons, and the amount and geometry of the surrounding cool materials. In a CV, for example, about half of the photons are typically intercepted by the WD surface, while additional fluorescence may occur in the accretion column (for an mCV), the accretion disk (non-magnetic CV), or the stellar envelope (SS). For the GRXE, however, the 6.4-keV line emission can be partly diffuse in origin, e.g., due to the fluorescence in dense ISM clouds or to their interaction with low-energy cosmic rays. Therefore, the GRXE can be used to place an upper limit to the overall population of 6.4-keV line-emitting sources in the Galaxy.

Various measurements of the Fe lines exist for local CVs, as well as for the GRXE. Probably the most extensive measurements for the GRXE are made by Uchiyama et al. (2013), who show that the EWs of the lines change systematically from the center to the ridge of the Galaxy. Toward the ridge, $EW_{6.4} = 110 \pm 10$ eV, $EW_{6.7} = 490 \pm 15$ eV, $EW_{7.0} = 110 \pm 10$ eV and $I_{7.0}/I_{6.7} = 0.2 \pm 0.08$; the errors of these EWs values were not given in Uchiyama et al. (2013) and are estimated from Yuasa et al. (2012), based on similar counting statistics of the lines, although the latter work was based on data collected for the Galactic bulge (specifically, observations taken in the Galactic longitude and latitude ranges $|l| \lesssim 3$ and $|b| \lesssim 2$, excluding the very central region of $|l| \lesssim 1$ and $|b| \lesssim 0.5$). The relative intensities of the lines change systematically from the ridge to the center; in particular, $I_{7.0}/I_{6.7} \approx 0.2$ in the ridge increases to ~ 0.25 in the budge, to ~ 0.4 in the center of the Galaxy. The $EW_{6.4}$ value varies strongly with position, especially in the central region, and sometimes with time (e.g., Yuasa et al. 2012; Munro et al. 2007). The $EW_{6.7}$ ($I_{7.0}/I_{6.7}$) values of the ridge appear to be significantly higher (lower) than those of relatively bright (but unidentified) sources (above $\sim 5 \times 10^{32}$ ergs s $^{-1}$ cm $^{-2}$)

detected by XMM (Warwick et al. 2014) and those of local mCVs (e.g., Ishida & Ezuk 1999; Uchiyama et al. 2013). Understanding this apparent inconsistency is a motivation of the work reported here.

We first systematically analyze the Fe emission line properties of local CVs and ABs and then confront the results with the measurements of the GRXE. The existing analyses of local CVs and ABs are rather inhomogeneous, based on data collected with various X-ray telescopes, such as *ASCA*, *Suzaku*, *Chandra HETG* and on different spectral modeling procedures. The sample sizes of the individual analyses are also small (typically less than 20 sources) (e.g., Ezuka & Ishida 1999; Hellier & Mukai 2004; Baskill et al. 2005; Rana et al. 2006; Schlegel et al. 2014). Our sample includes 41 CVs and 4 ABs, all observed with *Suzaku*. The results from our analysis of this sample can then directly be compared with similar *Suzaku* measurements of the GRXE (with minimum biases), providing new insights into the nature of the responsible source populations. The rest of the paper is organized as follows: In § 2 we describe our sample selection and data analysis methods; We present our results in § 3; We compare them with existing results and discuss the implications in § 4; And finally, in § 5, we provide a summary of the work.

2. Sample Selection & Data Analysis

Suzaku operated between 2005 and 2015. It had four X-ray Imaging Spectrometers (XIS): Three of them were made of front illuminated CCDs (XIS-0, -2 and -3), while the other of back-illuminated one (XIS-1). These spectrometers had the best spectral resolution ($E/\delta E \sim 20$ to 50) among the similar instruments that have operated in the 0.3-10 keV range. This high resolution is essential to the analysis reported here. The moderate spatial resolution of the instruments is also suited for local CVs and ABs: even though they are relatively bright sources, pile-ups are not an issue.

We cross-correlate the *Suzaku* online archive with Ritter & Kolb (2003)’s CV catalog and Eker et al. (2008)’s AB catalog to search for available observations. We find 48 publicly available observations on 41 CVs (including 6 SSs, 16 IPs, 3 polars and 16 DNe; multiple observations on several sources) and 4 observations on 4 ABs. The observation log of this source sample is presented in Table 1. One of the DNe, SS Cyg, was undergoing outburst during the observation. Nevertheless, it shows spectral properties similar to those of other DNe and is thus included in our subsequent analysis.

We reprocess the data downloaded from the *Suzaku* archive, using the software package *heasoft* (version 12.8.1; Arnaud 1996). Briefly, the event files are reduced with the standard pipeline routine *aepipeline* and the latest calibration files (XIS:20150312). For each observation, we extract an on-source spectrum and an off-source background spectrum, together with the response matrix (rmf) and effective area (arf) files, using *xselect*. The on-source spectrum is from a circular region with a typical radius $R = 200''$; however, it is reduced to $R = 120''$ to $150''$ for 20 observations, in which the sources are close to CCD edges. The background spectrum is from an annulus with the inner and outer radii equal to $\sim 250''$ and $400''$, except for the edges. Our results are not sensitive to the exact selection of the background area (which is always greater than the on-source region), because the sources are all quite bright.

We conduct the spectral analysis, using the *xspec* software package. The spectra from all XIS chips are jointly fitted to improve the counting statistics. Our focus is on the Fe emission lines and on the spectral shape of the continuum in the 5-10 keV range, which minimizes potential complications due to the thermal emission from the WD surfaces, as well as the absorption by the cold and warm gases at lower energies. Also in this range, the confusion from the emission from diffuse interstellar gas in the galactic disk is negligible (e.g., Yuasa et al. 2012). We model the continuum with the optically thin

thermal plasma model *apec* (with metallicity set to zero) for ease of comparison with previous results on GRXE (e.g., Yamauchi et al. 2009; Yuasa et al. 2012; Uchiyama et al. 2013). This modeling also gives a characteristic plasma temperature (T_b) for each source. We emphasize that T_b here is just used to characterize the hardness of the spectral continuum. The shock temperature T_{shock} in the cooling flow model (as used in Fig. 1) would be a more physical quantity comparing to T_b (e.g., when explaining $I_{7.0}/I_{6.7}$ - $EW_{6.7}$ anti-correlation in Fig. 4, see next section), but T_{shock} were not used to model the spectra of GRXE in previous works (e.g., Yamauchi et al. 2009; Yuasa et al. 2012; Uchiyama et al. 2013) and thus is not used in this work. A detailed analysis of the spectra of sampled sources with the cooling flow model is in preparation. We here mostly use $EW_{6.7}$ and $I_{7.0}/I_{6.7}$ as two independent line diagnostics of the plasma temperature. Accordingly, we construct a spectral model consisting of three Gaussians, representing the 6.4-keV, 6.7-keV and 7.0-keV lines. The parameters of this model include the centroid energies, widths, and (relative) intensities ($I_{6.4}/I_{6.7}$, $I_{6.7}$, and $I_{7.0}/I_{6.7}$) of the lines. Building the desirable relative intensities of the lines into the model (instead of using the standard normalizations of the individual Gaussians) automatically accounts for their correlations in error measurements. Additionally, the unabsorbed 2-10 keV flux and luminosity L_X of each source are calculated; the latter includes its error in the distance measurements (see Table 1).

For each class of our sample sources, we calculate the means and intrinsic dispersions of each individual parameter (T_b , $EW_{6.4}$, $EW_{6.7}$, $EW_{7.0}$, and $I_{7.0}/I_{6.7}$). For each class, we may construct an expected χ^2 statistic as

$$\chi^2 = \sum_{i=1}^n \frac{(x_i - a)^2}{b^2 + s_i^2}, \quad (1)$$

where n is the total source number, x_i and s_i are the measured value and error of the i -th source, whereas a and b are the expected mean and standard deviation of the parameter

(assuming a normal distribution). The χ^2 minimization relative to a gives the equation:

$$a = \sum_{i=1}^n \frac{x_i}{(b^2 + s_i^2)} / \sum_{i=1}^n \frac{1}{(b^2 + s_i^2)}. \quad (2)$$

This equation, together with setting χ^2 to its expected value $n - 2$ (the number of degrees of freedom), allows us to solve for a and b . The error of a can be further calculated from

$$\sigma^2 = \frac{1}{\sum_{i=1}^n [1/(s_i^2 + b^2)]}. \quad (3)$$

3. Results

Our main results are summarized in Table 2 and Fig 2 to Fig 8. Fig 3 to Fig 7 includes multiple measurements for sources with multiple observations (see Table 2 for details): SS73-17 (two measurements), XY Ari (two measurements) and VW Hyi (four measurements). Fig 2 shows the spectra, together with the best-fitted models, for four sources as an example for each CV class considered here. The most distinct differences among the spectra are the Fe line ratios: large $I_{7.0}/I_{6.7}$ and $I_{6.4}/I_{6.7}$ for mCVs (polars and IPs), large $EW_{6.7}$ for the DNe, and exceptionally enhanced 6.4-keV line intensity for the SSs. In general, the model fitting is acceptable, judged from the χ^2 values. Tables 2 and 3 summarize our results, while following figures illustrate trends and correlations among the measured parameters.

Fig 3 shows an apparent anti-correlation between $EW_{6.7}$ and T_b , which holds even for individual classes (though with lower significance). Classwise, IPs have the highest T_b (all above ~ 15 keV), while DNe have relatively low T_b (mostly below 15 keV); the mean T_b ratio is about 3, consistent with the expectation from the different accretion (and hence heating) processes between the two classes (§ 1). The polars tend to have lower temperatures, compared to IPs, which is also expected (due to the contribution from relatively soft cyclotron line emission; Longair 2011). Interestingly, none of the IPs has

$EW_{6.7}$ as high as the value measured for the GRXE! While a considerable fraction of DNe in our sample also have similarly small $EW_{6.7}$ (but with large error bars), the rest seem to be consistent with, or even significantly larger than, the GRXE value; these latter DNe tend to have low T_b . Not surprisingly, ABs tend to have the lowest T_b . But they are not necessarily high in $EW_{6.7}$ due to their relatively low metallicity (e.g., Berdyugina et al. 1998; Mallick 1998; Franciosini et al. 2001)

Fig. 4 shows $I_{7.0}/I_{6.7}$ vs. T_b of our sample sources. The correlation between these two parameters, as well as the $I_{7.0}/I_{6.7}$ values of individual classes, is consistent with the trends seen in Fig 3. Probably the only significant exception is EK TrA (a DN), which shows a low $I_{7.0}/I_{6.7}$, but a seemly high T_b , deviating from the overall correlation. But the ratio is consistent with the values of other DNe. As stated in § 1, the ratio is typically a more reliable temperature diagnostic than T_b or $EW_{6.7}$. If this is the case, then we may speculate the continuum of the source may be somewhat enhanced and hardened (to explain its high T_b and possibly slightly low $EW_{6.7}$ values, unusual for a DN; Fig 3). Again, none of the IPs are consistent with the GRXE in terms of the $I_{7.0}/I_{6.7}$ ratio. In general, IPs have higher T_b and higher $I_{7.0}/I_{6.7}$ values than DNe and ABs. The higher T_b values of IPs can be naturally explained by greater expected in-falling velocities at the stand shocks and therefore higher shock temperatures than in non-magnetic CVs (e.g., § 1; see also Longair 2011). A higher temperature also naturally leads to a larger Hydrogen-like Fe ion fraction, and therefore a higher $I_{7.0}/I_{6.7}$ value. The spectra of our sampled ABs generally do not show significant 7.0-keV lines, thus their $I_{7.0}/I_{6.7}$ are less than 0.2 (see Fig 4 and Fig 5 for details). As shown in Fig 5, the dependence of $I_{7.0}/I_{6.7}$ on $EW_{6.7}$ is consistent with the cooling flow model predictions.

Fig 6 compares $I_{6.4}/I_{6.7}$ with $I_{7.0}/I_{6.7}$ of our sample sources. As expected, there is a correlation between the two parameters, even for two individual classes, DNe and IPs.

Therefore, $I_{6.4}/I_{6.7}$ is also a reasonably good tracer of the hot plasma temperature for these classes. SSs, on the other hand, can have exceptionally stronger 6.4-keV line emission; three of them have $I_{6.4}/I_{6.7} \gtrsim 2.5$, which can be naturally explained by the presence of cool (fluorescing) material surrounding such systems.

Theoretically, one may also expect an anti-correlation of $EW_{6.7}$ with L_X or $I_{7.0}/I_{6.7}$. For a same accretion rate, the deeper the gravitational potential is (as traced by $EW_{6.7}$ and $I_{7.0}/I_{6.7}$), the higher L_X should be. Indeed, Fig 7 shows these expected correlations, most apparent when data points with large errors are discounted. All IPs, except for one, have $L_X > 10^{32}$ erg s $^{-1}$, while almost all DNe have $L_X < 10^{32}$ erg s $^{-1}$. The correlations are particularly convincing for DNe as a class with the Spearman’s rank order correlation coefficient $r_s = 0.65 \pm 0.17$. These correlations are not expected to be tight, because L_X also depends on the accretion rate, which could vary from one source to another of similar WD masses. Following the procedure described in Li & Wang (2013), we characterize the $EW_{6.7}$ - L_X correlation of DNe, using the best-fit log-log linear relation, $EW_{6.7} = (438 \pm 95 \text{ eV})(L/10^{31} \text{ ergs s}^{-1})^{(-0.31 \pm 0.15)}$ (Fig. 7). The root mean square of the data around the relation is $\approx 0.33 \pm 0.11$ dex.

Fig 8 shows that the GRXE (especially its $EW_{6.7}$ value) cannot be explained by any mixture of mCVs, SSs, and ABs, if our sample sources are representative of these individual classes. mCVs have higher T_b , lower $EW_{6.7}$ and higher $I_{7.0}/I_{6.7}$, compared to the GRXE. Similarly, ABs on average still have too low $EW_{6.7}$, but also too low $I_{7.0}/I_{6.7}$. In contrast, DNe have Fe lines properties consistent with those of the GRXE within $1\text{-}\sigma$. We discuss the implications of these results in the following section.

4. Discussion

The above spectral results are indicative as to the relative importance of the source classes responsible for the GRXE. However, to quantify their respective contributions, we need to be aware of the limitations of the results and to know the flux distributions of the source classes. To do so, we first compare our results with those from previous studies as a consistency check and then discuss the limitations and their effects as well as the ways to move forward.

4.1. Comparison to previous studies and common limitations

Various studies of local CVs and ABs have been carried out previously. The same *Suzaku* data on the IPs and SSs in our sample have mostly been analyzed; the results are quantitatively consistent with ours, in terms of T_b , as well as the Fe line equivalent widths (e.g., V1223 Sgr and V407 Cyg; Hayashi et al. 2011; Mukai et al. 2012). Only 8 of the CVs and 4 of the ABs are analyzed for the first time; they are marked in Table 1. All of these newly analyzed CVs are DNe, compared to eight studied previously (Ishida et al. 2009; Ikis et al. 2013; Mukai et al. 2009; Byckling et al. 2010; Saitou et al. 2012; Neustroev & Tsygankov 2014)). Some of our sample sources are included in existing *ASCA* studies, the results of which typically have large uncertainties. The EW uncertainty is typically ~ 40 eV in *ASCA* measurements (Ishida & Ezuk 1999; Ezuka & Ishida 1999), compared to ~ 10 eV in our *Suzaku* ones; the latter tend to have substantially higher signal to noise ratios, as well as the improved spectral resolution, than the former. Our results are also consistent with previous *Chandra* *HETG* measurements (e.g., for SS Cyg and U Gem, Rana et al. 2006; Schlegel et al. 2014). Recently, Eze (2015) compared the EWs of the 6.4 keV line of CVs to that of the GRXE based on a similar sample of SSs and mCVs, and conclude that SSs could account for the majority of the 6.4 keV line of GRXE. Our

measurements of EWs of Fe lines are in general consistent with theirs. However, their work mostly focused on 6.4 keV lines, and did not include DNe, thus did not address the question of main contributors of 6.7/7.0-keV lines of GRXE as was done in this paper. Therefore, our results, broadly consistent with the existing ones, represent a step forward in improving both the sample statistics and the uniformity of the data analysis, focusing on the Fe-line diagnostics.

There are various limitations in our results. First, the sample size of our studied sources remains small, especially for AB, SS, and Polar classes. Although they are unlikely to be major contributors to the observed 6.7-keV line emission of the GRXE (e.g., Fig. 8), their contributions to the 6.4-keV line (probably chiefly due to SSs) and to the soft X-ray continuum (from ABs) could be substantial, depending on their uncertain overall populations in the Galaxy. We thus focus our discussion on the relative roles of IPs and DNe, which are probably the two most important classes for explaining the 6.7 and 7.0 keV lines of the GRXE.

Second, the energy range effectively covered by the *Suzaku* data is limited. The energy coverage of XIS is mostly below 10 keV which brings uncertainties to temperature measurements. The hard X-ray detector (HXD) spectra, on the other hand, usually have sufficiently high signal-to-noise bins only up to ~ 40 keV, with typically only 2-3 bins above 20 keV. When the temperature of a plasma reaches above $\sim 20 - 40$ keV, the line diagnostics are also of little use, because atoms are almost fully ionized. Consequently, in such a case, the temperature cannot be well constrained. This limitation affects our ability to investigate the very hard part of the GRXE. Accordingly, we limit our discussion on the nature of the GRXE in the 2-10 keV band.

Third, our sample is certainly very incomplete and biased toward relatively bright sources. The sampling is probably reasonable for IPs and perhaps SSs, which tend to have

high luminosities, but is clearly inadequate for DNe and ABs. Only five sources in eight observations in our sample are less luminous than 10^{31} erg s $^{-1}$ (Fig. 7). Therefore, the line or temperature measurements based on the sample may not be representative. In such a case (e.g., for DNe), the luminosity-dependence of the measurements must be accounted for.

4.2. Integrated DNe contribution to the GRXE

To quantify the contribution of DNe to the GRXE, we need to know their LF. Indeed, the LFs of local CVs and ABs have been studied; the statistics of DNe, which are mostly below several 10^{31} erg s $^{-1}$, remains too poor to be analyzed separately (Sazonov et al. 2006). Byckling et al. (2010); Pretorius & Knigge (2012); Reis et al. (2013) suggest the presence of a faint population of DNe below 10^{31} erg s $^{-1}$ and a LF with $\frac{dN}{dL} \propto L^{-1.64}$; however, their sample sizes are also not large enough to put tight constraints on LF parameters, and the slope of the LF is inconsistent with that of the GRXE sources ($\frac{dN}{dL} \propto L^{-2.5}$, tighter constraints could be put to the LF of local DNe though, see discussion below). Here we use the well-constrained LF of X-ray sources directly observed in the limited window (Revnivtsev et al. 2009): $\frac{dN}{dL} \propto L^{-2.5}$. This LF extends to the luminosity limit of $\sim 10^{30}$ erg s $^{-1}$. Between this limit and $L \sim 10^{31}$ erg s $^{-1}$, the sources should mostly be DNe. Sources below 10^{30} ergs s $^{-1}$, as suggested by Byckling et al. (2010); Pretorius & Knigge (2012); Reis et al. (2013), could be populous and contribute a negligible part of the GRXE. However, they are unlikely to dominate GRXE, because sources above 10^{30} ergs s $^{-1}$ contribute more than 80% of GRXE(Revnivtsev et al. 2009), which leaves only 20% for fainter sources. Nevertheless, detailed investigation on their Fe line properties are necessary to confirm their relative importance. We will thus concentrate on sources between 10^{30-32} ergs s $^{-1}$. Our objective here is to demonstrate how the luminosity-dependence affects the measurements of $EW_{6.7}$.

We calculate the LF-accumulated $EW_{6.7,A}$ as

$$EW_{6.7} = \frac{\int_{L_{min}}^{L_{max}} EW_{6.7} L \frac{dN}{dL} dL}{L_A}, \quad (4)$$

where the continuum at 6.7 keV is assumed to be scaled with L and

$$L_A = \int \frac{dN}{dL} L dL. \quad (5)$$

We account for the $EW_{6.7}$ dependence on L using the best-fit relation obtained in § 3.

If we take the upper and lower luminosity limits of the integration as 10^{32} ergs s $^{-1}$ and 10^{30} ergs s $^{-1}$, to match the luminosity range of the observed LF and DNe, the resulting $EW_{6.7}$ is 540^{+79}_{-88} eV (or 448^{+60}_{-65} eV if the upper luminosity limit taken to 10^{34} ergs s $^{-1}$), which is consistent with, or slightly greater than the measured GRXE value. An excess of the DN $EW_{6.7}$ value is indeed needed to balance the contributions from mCVs and ABs, which have substantially lower $EW_{6.7}$ values ($EW_{6.7}$ below 300 eV, see Table 3.).

Conversely, we can use the observed $EW_{6.7} = 490 \pm 15$ eV value of the GRXE to place constraints on the LF slope of local DNe by integrating EQ. 4, if we assume CVs in both environments share similar $EW_{6.7}$ values. To reach a $EW_{6.7} = 490 \pm 15$ eV, the LF has to be steeper than -2.25 over the $10^{30} - 10^{34}$ ergs s $^{-1}$ range. Of course, accounting for contributions from other source populations would require a steeper LF and/or an even lower luminosity limit of DNe. Therefore, our results are consistent with the presence of a large population of local DNe with individual luminosities below 10^{31} ergs s $^{-1}$, (more than ten times more numerous than those above 10^{31} ergs s $^{-1}$; Byckling et al. (2010); Pretorius & Knigge (2012); Reis et al. (2013)), but requires a steeper LF which needs to be confirmed by further observations.

4.2.1. Contributions from other sources

We have focused on the Fe emission lines and their constraints on the nature of the sources responsible for the GRXE. As shown in Fig. 1, the lines are good diagnostics of the shock temperature (for the cooling flow model) up to about 20-40 keV. The line emission saturates at higher temperatures (e.g., $EW_{6.7}$ predicted by cooling flow model hardly changes above 40 keV, and $EW_{6.7}$ by *apec* model drops below 10 eV, which is hard to be measured; meanwhile, $I_{7.0}/I_{6.7}$ of cooling flow model becomes flatter and that of *apec* model starts dropping above 40 keV). This saturation is the reason that mCVs cannot be the major contributor to the strong line emission observed in the GRXE. However, its hard X-ray continuum spectrum is likely dominated by mCVs.

As shown in Fig. 3, mCVs (especially IPs) typically have $T_b > 15$ keV, higher than the characteristic temperature of the GRXE in the 2-50 keV band (Yuasa et al. 2012). Because T_b is lower than T_{shock} in the cooling-flow spectral model of mCVs, their mean continuum shape should be harder than that indicated by the one-temperature characterization. Such a hard continuum contribution from mCVs can naturally be balanced by the soft mean spectra of DNe and ABs, which all have characteristic temperatures lower than 15 keV.

In short, while a quantitative decomposition of the GRXE into the contributions from specific X-ray source classes is still beyond the scope of the present study, it is clear that their relative importances are different for the Fe lines and for the hard spectral continuum.

5. Summary

We have systematically analyzed of the *Suzaku* spectra of 45 local CVs and ABs to explore the significance of their contributions to the GRXE. This sample consists of 6 SSs, 16 IPs, 3 polars, 16 DNe and 4 ABs. The data for 12 of these sources are analyzed for the

first time. Our main results and conclusions are as follows:

- Our measurements are focused on the Fe 6.4, 6.7, 7.0-keV lines, which are used as temperature diagnostics of the X-ray-emitting optically-thin thermal plasma. We find that the mean EW of the 6.7-keV line decreases from $\sim 438(286)$ eV for DNe (ABs) to ~ 107 eV for IPs. In contrast, the line flux ratio $I_{7.0}/I_{6.7}$ increases from ~ 0.27 for DNe to ~ 0.71 for IPs. Such trends are well consistent with the expected higher temperature plasma in IPs due to the greater in-falling velocities of accreted matter than in DNe of similar WD masses. We also find that $I_{6.4}/I_{6.7}$ is strongly correlated with $I_{7.0}/I_{6.7}$ (except for the SSs), consistent with the expectation that the 6.4-keV line also traces the Fe-ionizing photon fluxes and hence the plasma temperature.
- All sources classes considered here, except for DNe, show average Fe-line diagnostics ($EW_{6.7}$ and $I_{7.0}/I_{6.7}$) significantly different from those observed in the GRXE. Thus, DNe, though relatively faint (10^{30-32} erg s $^{-1}$ in our sampled range), are the most likely class accounting for the bulk of the 6.7-keV and 7.0-keV line intensities observed in the GRXE. In particular, we find a strong correlation between $EW_{6.7}$ and L , which can be characterized by the relation $EW_{6.7} = (438 \pm 95 \text{ eV})(L/10^{31} \text{ ergs s}^{-1})^{(-0.31 \pm 0.15)}$. This correlation indicates that the bulk of the emission arises from faint DNe.
- Without a major contribution from DNe, no combination of other source classes seems to be able to explain the observed 6.7-keV and 7.0-keV line intensities of the GRXE. These classes, however, can be major contributors to other parts of the GRXE. In particular, IPs can dominate in the harder band. IPs are in general brighter than 10^{32} erg s $^{-1}$. Therefore, relatively bright sources observed in the GRXE tend to be mCVs. Conversely, ABs may be significant in contributing to the soft X-ray continuum.

These results demonstrate the diagnostic power of the Fe emission lines. In comparison with the overall X-ray spectral shape, the EWs of the lines or their ratios provide more direct probes of the X-ray-emitting plasma in the intermediate temperature range of $\sim 1 - 20$ keV and are less sensitive to complications such as the metallicity of the plasma, as well as the reflection and absorption of X-rays. The observed lines of the GRXE can therefore be used as the fundamental constraints and limits on the nature and population of the underlying responsible source classes.

The authors thank the anonymous referee for constructive comments that helped improve this paper. WQD appreciate valuable discussions with K. Mukai and T. Yuasa during the course of this work. This work is partly supported by National Science Foundation of China through grants NSFC-11303015 and NSFC-11133001.

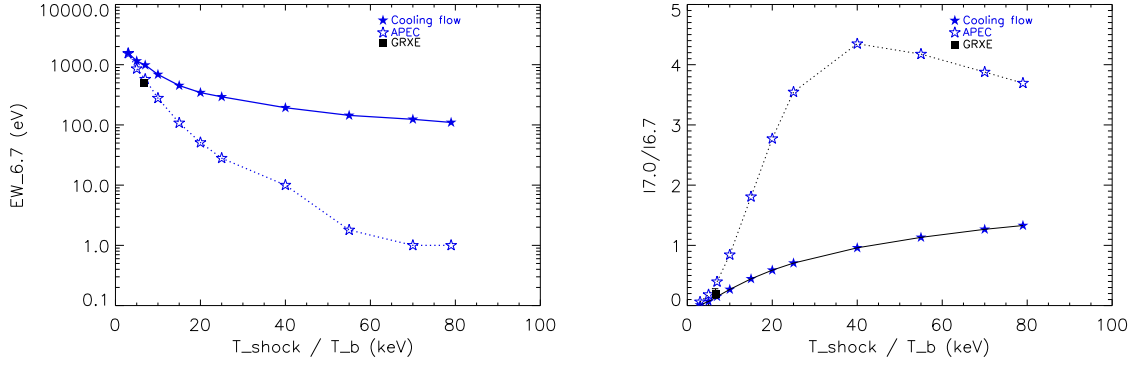


Fig. 1.— $EW_{6.7}$ (left panel) and $I_{7.0}/I_{6.7}$ (right panel) as function of the plasma or shock temperature for two spectral models. $EW_{6.7}$ is proportional to the Fe abundances (the solar value is assumed here; Gray e.g., 2008). The measured T_b , $EW_{6.7}$ and $I_{7.0}/I_{6.7}$ (Uchiyama et al. 2013) for the GRXE are marked for reference.

Table 1: Basic information of sampled CVs & ABs.

Source	Class	Obs-ID	D	F_{2-10}	L	References
			(kpc)	$10^{-12} \text{ erg s}^{-1} \text{ cm}^{-2}$	$10^{31} \text{ erg s}^{-1}$	
CH Cyg ₁	SS	400016020	$0.268^{+0.066}_{-0.066}$	3.89	$3.35^{+1.85}_{-1.44}$	Perryman et al. (1997)
CH Cyg ₂	SS	400016030	$0.268^{+0.066}_{-0.066}$	3.91	$3.36^{+1.86}_{-1.45}$	Perryman et al. (1997)
RS Oph	SS	406033010	$1.4^{+0.6}_{-0.2}$	2.71	$63.7^{+66.3}_{-16.9}$	Barry et al. (2008)
RT Cru	SS	402040010	—	30.0	—	—
SS73-17 ₁	SS	401055010	$0.5^{+0.5}_{-0.25}$	17.2	$51.7^{+155}_{-38.8}$	Perryman et al. (1997)
SS73-17 ₂	SS	403043010	$0.5^{+0.5}_{-0.25}$	15.6	$46.7^{+140}_{-35.0}$	Perryman et al. (1997)
T Crb	SS	401043010	—	36.1	—	—
V407 Cyg	SS	905001010	—	6.99	—	—
AO Psc	IP	404033010	$0.33^{+0.18}_{-0.12}$	4.86	$63.4^{+88.1}_{-37.7}$	Pretorius & Mukai (2014)
BG Cmi	IP	404029010	—	23.0	—	—
EX Hya	IP	402001010	$0.065^{+0.001}_{-0.001}$	81.7	$4.13^{+0.13}_{-0.13}$	Godon et al (2012)
FO Aqr	IP	404032010	$0.45^{+0.24}_{-0.16}$	47.6	$115^{+156}_{-67.5}$	Pretorius & Mukai (2014)
IGR J17195-4100	IP	403028010	—	34.3	—	—
IGR J17303-0601	IP	403026010	—	17.9	—	—
MU Cam	IP	403004010	—	9.65	—	—
NY Lup	IP	401037010	$0.68^{+0.17}_{-0.13}$	29.6	164^{+91}_{-57}	de Martino et al. (2006)
PQ Gem	IP	404030010	$0.51^{+0.28}_{-0.18}$	21.9	$68.1^{+95.4}_{-39.6}$	Pretorius & Mukai (2014)
1RXS J213344.1+51072	IP	401038010	—	20.1	—	—
TV Col	IP	403023010	$0.368^{+0.017}_{-0.015}$	49.5	$80.1^{+7.57}_{-6.40}$	Ozdonmez et al. (2015)
TX Col	IP	404031010	—	10.8	—	—
V1223 Sgr	IP	402002010	$0.527^{+0.054}_{-0.043}$	95.6	$317^{+68.4}_{-49.7}$	Ozdonmez et al. (2015)
V2400 Oph	IP	403021010	$0.28^{+0.15}_{-0.10}$	44.9	$42.1^{+57.2}_{-24.7}$	Barlow et al. (2006)
V709 Cas	IP	403025010	$0.230^{+0.020}_{-0.020}$	35.5	$22.5^{+4.08}_{-3.74}$	Barlow et al. (2006)
XY Ari ₁	IP	500015010	$0.27^{+0.1}_{-0.1}$	18.8	$16.4^{+14.4}_{-9.89}$	Pretorius & Mukai (2014)
XY Ari ₂	IP	506026010	$0.27^{+0.1}_{-0.1}$	20.0	$17.5^{+15.4}_{-10.6}$	Pretorius & Mukai (2014)
SWIFT J2319.4+2619	Po	408030010	—	3.08	—	—
AM Her	Po	403007010	$0.091^{+0.018}_{-0.015}$	0.350	$0.034^{+0.015}_{-0.013}$	Gansicke (1995)
V1432 Aql	Po	403027010	0.23	26.7	16.9 ± 0.3	Watson (1995)
BF Eri ^a	DN	407045010	$0.7^{+0.2}_{-0.2}$	1.33	$7.79^{+5.09}_{-3.82}$	Neustroev & Zharikov (2008)
BV Cen ^a	DN	407047010	0.238	14.1	9.54 ± 0.2	Godon et al (2012)
BZ UMa	DN	402046010	$0.228^{+0.063}_{-0.043}$	2.79	$1.73^{+1.09}_{-0.59}$	Thorstensen et al. (2008)
EK TrA ^a	DN	407044010	0.18	4.09	1.58 ± 0.1	Gansicke et al. (1997)
FL Psc ^a	DN	403039010	—	0.396	—	—
FS Aur	DN	408041010	—	2.53	—	—
GK Per ^a	DN	403081010	0.420	7.26	15.3 ± 0.2	Pretorius & Mukai (2014)
KT Per	DN	403041010	$0.145^{+0.030}_{-0.021}$	2.82	$0.708^{+0.321}_{-0.191}$	Thorstensen et al. (2008)
SS Aur	DN	402045010	$0.201^{+0.010}_{-0.010}$	2.99	$1.45^{+0.14}_{-0.14}$	Ozdonmez et al. (2015)
SS Cyg	DN	400007010	0.166	14.6	4.81 ± 0.04	Ozdonmez et al. (2015)
U Gem ₁	DN	407034010	$0.1^{+0.004}_{-0.004}$	12.5	$1.50^{+0.13}_{-0.11}$	Ozdonmez et al. (2015)
U Gem ₂	DN	407035010	$0.1^{+0.004}_{-0.004}$	5.56	$0.665^{+0.054}_{-0.052}$	Ozdonmez et al. (2015)
V1159 Ori ^a	DN	408029010	—	1.00	—	—
V893 Sco	DN	401041010	$0.135^{+0.063}_{-0.032}$	19.9	$4.34^{+5.00}_{-1.82}$	Ozdonmez et al. (2015)
VW Hyi ₁ ^a	DN	406009010	$0.064^{+0.020}_{-0.017}$	1.44	$0.071^{+0.051}_{-0.032}$	Pretorius & Knigge (2012)
VW Hyi ₂ ^a	DN	406009020	$0.064^{+0.020}_{-0.017}$	5.86	$0.287^{+0.207}_{-0.133}$	Pretorius & Knigge (2012)
VW Hyi ₃ ^a	DN	406009030	$0.064^{+0.020}_{-0.017}$	4.96	$0.243^{+0.175}_{-0.112}$	Pretorius & Knigge (2012)
VW Hyi ₄ ^a	DN	406009040	$0.064^{+0.020}_{-0.017}$	5.20	$0.255^{+0.301}_{-0.117}$	Pretorius & Knigge (2012)
VY Aqr ^a	DN	402043010	$0.097^{+0.015}_{-0.012}$	1.08	$0.122^{+0.41}_{-0.28}$	Ozdonmez et al. (2015)
Z Cam	DN	404022010	$0.163^{+0.068}_{-0.038}$	27.4	$8.69^{+8.71}_{-3.58}$	Ozdonmez et al. (2015)
GT Mus ^a	AB	402095010	—	7.13	—	—
II Peg ^a	AB	407038010	—	2.30	—	—
σ Gem ^a	AB	402033010	—	1.01	—	—
UX Ari ^a	AB	404008010	—	1.51	—	—

Note: ^aSources firstly analyzed in this paper.

Table 2: Fitting results for individual sources

Source	Class	T_b	$EW_{6.4}$	$I_{6.4}/I_{6.7}$	$E_{6.7}$	$I_{6.7}$	$EW_{6.7}$	$EW_{7.0}$	$I_{7.0}/I_{6.7}$	$\chi^2/\text{d.o.f.}$
		(keV)	eV		(eV)		(eV)	(eV)		
CH Cyg ₁	SS	200 ^{+0.0} _{-54.6}	390 ⁺⁸⁸ ₋₈₅	2.91 ^{+0.64} _{-0.42}	6.56 ^{+0.04} _{-0.03}	16.9 ^{+2.31} _{-2.78}	532 ⁺¹⁰⁴ ₋₈₃	76 ⁺⁴⁰ ₋₄₀	0.56 ^{+0.25} _{-0.11}	1.52/191
CH Cyg ₂	SS	8.38 ^{+2.97} _{-1.83}	839 ⁺⁹⁰ ₋₆₈	2.82 ^{+0.53} _{-0.41}	6.62 ^{+0.02} _{-0.02}	30.4 ^{+4.26} _{-4.12}	92 ⁺²² ₋₁₈	117 ⁺³² ₋₃₅	0.33 ^{+0.10} _{-0.09}	1.05/172
RS Oph	SS	3.46 ^{+40.8} _{-2.20}	82 ⁺¹⁹³ ₋₈₂	2.72 ^{+2.57} _{-1.07}	6.71 ^{+0.09} _{-0.09}	5.28 ^{+2.51} _{-2.60}	630 ⁺⁶⁰⁶ ₋₁₉₁	165 ⁺²⁴⁴ ₋₆₂	0.22 ^{+0.52} _{-0.22}	0.91/49
RT Cru	SS	53.1 ^{+8.61} _{-5.17}	200 ⁺¹³ ₋₁₃	1.65 ^{+0.18} _{-0.15}	6.673 ^{+0.01} _{-0.01}	48.0 ^{+4.76} _{-4.97}	88 ⁺⁸ ₋₉	70 ⁺⁹ ₋₁₁	0.57 ^{+0.11} _{-0.09}	1.06/942
SS73-17 ₁	SS	8.33 ^{+2.73} _{-1.74}	176 ⁺²⁰ ₋₂₀	1.06 ^{+0.16} _{-0.15}	6.664 ^{+0.01} _{-0.01}	79.9 ^{+11.0} _{-8.47}	160 ⁺¹⁷ ₋₁₉	109 ⁺²² ₋₂₆	0.51 ^{+0.11} _{-0.10}	1.02/423
SS73-17 ₂	SS	13.25 ^{+8.34} _{-3.04}	291 ⁺³⁵ ₋₃₃	0.96 ^{+0.20} _{-0.15}	6.69 ^{+0.01} _{-0.02}	50.6 ^{+9.41} _{-9.13}	145 ⁺²² ₋₂₁	133 ⁺³⁶ ₋₂₆	0.54 ^{+0.13} _{-0.11}	0.88/219
T Crb	SS	34.6 ^{+3.08} _{-2.72}	161 ⁺¹⁰ ₋₁₀	1.48 ^{+0.17} _{-0.14}	6.70 ^{+0.01} _{-0.01}	52.7 ^{+5.15} _{-5.15}	87 ⁺⁸ ₋₉	123 ⁺¹³ ₋₁₂	0.83 ^{+0.12} _{-0.10}	0.97/1229
V407 Cyg	SS	3.96 ^{+0.69} _{-0.53}	104 ⁺¹⁰ ₋₁₀₄	0.05 ^{+0.09} _{-0.05}	6.67 ^{+0.01} _{-0.01}	18.1 ^{+5.15} _{-5.15}	418 ⁺⁵⁸ ₋₅₁	0 ⁺¹⁰ ₋₀	0.03 ^{+0.08} _{-0.03}	1.10/116
AO Psc	IP	19.7 ^{+3.26} _{-2.49}	158 ⁺¹⁵ ₋₁₅	0.68 ^{+0.07} _{-0.06}	6.67 ^{+0.01} _{-0.01}	114.8 ^{+7.16} _{-7.52}	174 ⁺¹⁴ ₋₁₃	100 ⁺¹⁰ ₋₁₀	0.56 ^{+0.06} _{-0.06}	0.969/1262
BG Cmi	IP	42.6 ^{+6.55} _{-5.34}	102 ⁺¹⁵ ₋₁₆	1.18 ^{+0.30} _{-0.19}	6.65 ^{+0.02} _{-0.02}	23.9 ^{+3.55} _{-3.63}	81 ⁺¹⁴ ₋₁₂	54 ⁺¹⁴ ₋₁₃	0.57 ^{+0.18} _{-0.14}	1.04/934
EX Hya lines	IP	9.41 ^{+0.40} _{-0.38}	32 ⁺³ ₋₃	0.13 ^{+0.01} _{-0.01}	6.67 ^{+0.01} _{-0.01}	310.6 ^{+5.39} _{-5.39}	325 ⁺⁶ ₋₇	110 ⁺⁴ ₋₄	0.39 ^{+0.02} _{-0.01}	1.03/3100
FO Aqr	IP	19.1 ^{+2.88} _{-2.28}	133 ⁺⁹ ₋₉	1.75 ^{+0.24} _{-0.19}	6.66 ^{+0.02} _{-0.01}	60.3 ^{+6.21} _{-6.24}	73 ⁺⁸ ₋₈	58 ⁺¹⁰ ₋₁₁	0.58 ^{+0.12} _{-0.12}	0.94/1841
IGR J17195-4100	IP	30.5 ^{+8.94} _{-6.06}	128 ⁺¹⁰ ₋₁₁	1.26 ^{+0.20} _{-0.17}	6.68 ^{+0.01} _{-0.01}	45.0 ^{+5.06} _{-4.94}	91 ⁺¹⁰ ₋₁₀	32 ⁺² ₋₃	0.87 ^{+0.26} _{-0.14}	0.98/1131
IGR J17303-0601	IP	63.6 ^{+64.8} _{-24.0}	88 ⁺³⁵ ₋₂₄	1.50 ^{+0.99} _{-0.71}	6.54 ^{+0.05} _{-0.08}	14.8 ^{+4.07} _{-5.51}	59 ⁺¹⁵ ₋₁₈	62 ⁺²¹ ₋₁₆	0.92 ^{+0.66} _{-0.30}	0.91/721
MU Cam	IP	15.8 ^{+4.07} _{-3.04}	139 ⁺¹⁷ ₋₁₆	1.21 ^{+0.25} _{-0.19}	6.67 ^{+0.01} _{-0.01}	23.0 ^{+3.07} _{-3.07}	101 ⁺¹⁴ ₋₁₃	134 ⁺¹⁸ ₋₁₇	0.94 ^{+0.21} _{-0.16}	0.93/631
NY Lup	IP	43.5 ^{+11.76} _{-7.53}	156 ⁺⁷ ₋₇	1.17 ^{+0.12} _{-0.07}	6.67 ^{+0.01} _{-0.01}	54.8 ^{+2.89} _{-2.89}	116 ⁺⁷ ₋₆	120 ⁺⁷ ₋₇	0.81 ^{+0.08} _{-0.07}	0.99/2319
PQ Gem	IP	32.6 ^{+12.7} _{-7.71}	128 ⁺¹⁴ ₋₁₄	1.93 ^{+0.57} _{-0.36}	6.65 ^{+0.02} _{-0.02}	17.7 ^{+3.47} _{-3.49}	58 ⁺¹⁰ ₋₁₃	62 ⁺¹² ₋₁₃	0.77 ^{+0.30} _{-0.22}	1.05/938
1RXS J213344.1+51072	IP	65.9 ^{+18.3} _{-13.3}	172 ⁺¹⁰ ₋₁₂	1.83 ^{+0.24} _{-0.19}	6.69 ^{+0.01} _{-0.02}	24.9 ^{+2.66} _{-2.56}	79 ⁺⁸ ₋₉	91 ⁺¹¹ ₋₁₀	0.88 ^{+0.14} _{-0.07}	1.07/1429
TV Col	IP	40.5 ^{+12.9} _{-8.28}	120 ⁺⁹ ₋₁₁	0.86 ^{+0.06} _{-0.08}	6.67 ^{+0.01} _{-0.01}	92.1 ^{+6.40} _{-6.21}	131 ⁺⁸ ₋₈	104 ⁺¹⁰ ₋₁₁	0.67 ^{+0.08} _{-0.04}	1.14/1403
TX Col	IP	26.9 ^{+6.10} _{-7.19}	88 ⁺¹⁵ ₋₁₅	0.71 ^{+0.16} _{-0.15}	6.68 ^{+0.01} _{-0.01}	18.5 ^{+2.37} _{-2.45}	121 ⁺¹⁶ ₋₁₉	94 ⁺²⁰ ₋₁₇	0.69 ^{+0.18} _{-0.14}	0.92/626
V1223 Sgr	IP	26.6 ^{+4.40} _{-3.47}	97 ⁺⁶ ₋₅	1.29 ^{+1.11} _{-0.09}	6.67 ^{+0.01} _{-0.01}	110.5 ^{+7.02} _{-7.02}	71 ⁺⁵ ₋₅	70 ⁺⁶ ₋₇	0.80 ^{+0.08} _{-0.08}	1.04/3000
V2400 Oph	IP	22.8 ^{+2.01} _{-1.78}	140 ⁺⁶ ₋₆	1.24 ^{+0.07} _{-0.06}	6.67 ^{+0.01} _{-0.01}	65.8 ^{+2.96} _{-2.96}	102 ⁺⁵ ₋₅	93 ⁺⁷ ₋₆	0.73 ^{+0.05} _{-0.05}	1.05/2992
V709 Cas	IP	47.3 ^{+6.50} _{-5.07}	131 ⁺¹¹ ₋₁₀	1.98 ^{+0.39} _{-0.26}	6.67 ^{+0.02} _{-0.01}	29.5 ^{+4.30} _{-4.18}	60 ⁺⁸ ₋₉	69 ⁺¹¹ ₋₁₁	0.92 ^{+0.23} _{-0.18}	1.02/1397
XY Ari ₁	IP	39.6 ^{+13.1} _{-8.21}	70 ⁺⁸ ₋₈	0.76 ^{+0.11} _{-0.10}	6.67 ^{+0.01} _{-0.01}	24.6 ^{+2.29} _{-2.23}	94 ⁺⁹ ₋₈	57 ⁺⁸ ₋₉	0.54 ^{+0.10} _{-0.09}	0.97/1454
XY Ari ₂	IP	31.6 ^{+13.2} _{-8.46}	80 ⁺¹⁶ ₋₁₂	0.84 ^{+0.12} _{-0.11}	6.66 ^{+0.01} _{-0.01}	24.1 ^{+1.83} _{-1.83}	91 ⁺¹⁴ ₋₁₃	65 ⁺¹¹ ₋₉	0.62 ^{+0.11} _{-0.10}	0.90/1823
SWIFT J2319.4+2619	Po	9.02 ^{+4.80} _{-2.28}	90 ⁺⁵² ₋₃₂	0.46 ^{+0.23} _{-0.19}	6.65 ^{+0.03} _{-0.03}	8.34 ^{+1.57} _{-1.72}	208 ⁺⁸⁰ ₋₄₄	119 ⁺⁴⁶ ₋₃₅	0.53 ^{+0.26} _{-0.20}	0.89/184
AM Her	Po	8.42 ^{+3.08} _{-2.09}	0.0 ^{+0.01} _{-0.0}	0.0 ^{+0.09} _{-0.0}	6.63 ^{+0.04} _{-0.04}	1.35 ^{+0.48} _{-0.48}	454 ⁺¹⁷⁸ ₋₁₈₂	43 ⁺¹³³ ₋₄₃	0.09 ^{+0.37} _{-0.09}	1.11/112
V1432 Aql	Po	16.7 ^{+3.01} _{-2.28}	110 ⁺¹⁰ ₋₁₂	1.08 ^{+0.18} _{-0.15}	6.67 ^{+0.01} _{-0.01}	46.9 ^{+5.12} _{-5.07}	99 ⁺¹² ₋₉	63 ⁺¹³ ₋₁₂	0.51 ^{+0.12} _{-0.11}	0.90/1052
BF Eri	DN	3.56 ^{+2.21} _{-1.20}	223 ⁺⁶⁶⁰ ₋₁₄₀	0.0 ^{+0.0} _{-0.0}	6.75 ^{+0.16} _{-0.16}	0.69 ^{+0.96} _{-0.60}	87 ⁺¹²³ ₋₈₇	0.0 ^{+0.0} _{-0.0}	0.0 ^{+0.31} _{-0.0}	0.95/53
BV Cen	DN	13.3 ^{+4.82} _{-2.77}	68 ⁺²¹ ₋₁₆	0.26 ^{+0.07} _{-0.06}	6.67 ^{+0.01} _{-0.01}	46.8 ^{+3.66} _{-3.80}	279 ⁺²⁶ ₋₂₈	151 ⁺²² ₋₁₇	0.53 ^{+0.09} _{-0.08}	0.92/498
BZ UMa	DN	5.12 ^{+5.23} _{-1.94}	76 ⁺⁴⁹ ₋₄₀	0.22 ^{+0.15} _{-0.12}	6.67 ^{+0.02} _{-0.02}	9.99 ^{+1.77} _{-1.87}	433 ⁺⁹⁴ ₋₈₄	153 ⁺⁵⁸ ₋₅₃	0.40 ^{+0.17} _{-0.15}	0.87/74
EK TrA	DN	38.8 ^{+35.4} _{-14.7}	197 ⁺⁶⁰ ₋₅₅	0.11 ^{+0.08} _{-0.07}	6.67 ^{+0.01} _{-0.01}	20.0 ^{+2.46} _{-2.49}	45 ⁺³¹ ₋₃₄	512 ⁺¹³⁵ ₋₈₀	0.16 ^{+0.08} _{-0.08}	0.97/114
FL Psc	DN	8.46 ^{+34.9} _{-4.55}	76 ⁺³⁴⁰ ₋₇₆	0.16 ^{+0.61} _{-0.16}	6.69 ^{+0.01} _{-0.01}	2.93 ^{+0.98} _{-0.98}	920 ⁺⁶⁶⁰ ₋₅₁₁	46 ⁺²⁰⁰ ₋₄₆	0.10 ^{+0.57} _{-0.10}	0.78/51
FS Aur	DN	15.9 ^{+17.5} _{-6.08}	52 ⁺³⁵ ₋₂₈	0.32 ^{+0.23} _{-0.18}	6.67 ^{+0.03} _{-0.03}	5.16 ^{+1.09} _{-1.13}	189 ⁺⁶⁷ ₋₅₁	76 ⁺⁴⁷ ₋₃₅	0.40 ^{+0.24} _{-0.19}	0.97/252
GK Per	DN	13.6 ^{+8.95} _{-3.96}	37 ⁺³⁵ ₋₃₁	1.06 ^{+0.78} _{-0.45}	6.65 ^{+0.08} _{-0.08}	6.47 ^{+2.47} _{-2.42}	70 ⁺³⁰ ₋₂₆	78 ⁺³³ ₋₃₀	0.94 ^{+0.76} _{-0.45}	1.13/210
KT Per	DN	10.3 ^{+12.8} _{-3.82}	77 ⁺³³ ₋₃₆	0.16 ^{+0.18} _{-0.16}	6.71 ^{+0.20} _{-0.38}	4.73 ^{+4.47} _{-4.34}	157 ⁺¹⁵⁵ ₋₁₃₃	25 ⁺⁵⁷ ₋₂₅	0.10 ^{+0.18} _{-0.10}	0.85/118
SS Aur	DN	8.48 ^{+5.34} _{-2.61}	47 ⁺²⁹ ₋₂₉	0.17 ^{+0.15} _{-0.13}	6.66 ^{+0.02} _{-0.02}	14.0 ^{+2.66} _{-2.67}	325 ⁺⁹⁰ ₋₆₅	169 ⁺⁵⁷ ₋₄₉	0.56 ^{+0.23} _{-0.18}	0.89/84
SS Cyg	DN	8.15 ^{+1.23} _{-0.91}	67 ⁺¹¹ ₋₁₀	0.30 ^{+0.05} _{-0.04}	6.67 ^{+0.01} _{-0.01}	57.1 ^{+2.89} _{-2.88}	415 ⁺⁴¹ ₋₃₀	48 ⁺¹⁵ ₋₁₁	0.16 ^{+0.04} _{-0.04}	1.12/773
U Gem ₁	DN	16.5 ^{+4.49} _{-3.31}	43 ⁺¹⁶ ₋₁₁	0.19 ^{+0.05} _{-0.05}	6.67 ^{+0.01} _{-0.01}	19.4 ^{+1.27} _{-1.30}	258 ⁺²² ₋₂₁	178 ⁺¹¹ ₋₁₁	0.68 ^{+0.08} _{-0.08}	0.97/839
U Gem ₂	DN	9.55 ^{+1.54} _{-1.16}	94 ⁺¹³ ₋₁₄	0.30 ^{+0.06} _{-0.04}	6.67 ^{+0.01} _{-0.01}	64.5 ^{+3.22} _{-3.84}	420 ⁺²⁷ ₋₂₉	100 ⁺¹³ ₋₁₄	0.28 ^{+0.04} _{-0.04}	1.06/690
V1159 Ori	DN	6.97 ^{+2.22} _{-1.83}	40 ⁺⁴⁸ ₋₈	0.15 ^{+0.17} _{-0.15}	6.66 ^{+0.07} _{-0.08}	2.87 ^{+0.42} _{-0.42}	331 ⁺¹⁰⁵ ₋₄₇	45 ⁺⁶⁸ ₋₆	0.14 ^{+0.17} _{-0.14}	0.94/181
V893 Sco	DN	9.36 ^{+1.59} _{-1.21}	51 ⁺¹⁴ ₋₁₁	0.19 ^{+0.05} _{-0.05}	6.69 ^{+0.01} _{-0.01}	75.3 ^{+5.07} _{-4.98}	351 ⁺³⁷ ₋₃₈	110 ⁺¹⁹ ₋₁₅	0.37 ^{+0.06} _{-0.06}	0.91/558
VW Hyi ₁	DN	5.79 ^{+4.71} _{-2.14}	0 ^{+0.01} ₋₀	0.08 ^{+0.07} _{-0.06}	6.65 ^{+0.02} _{-0.01}	9.3 ^{+1.01} _{-1.00}	1392 ⁺¹⁵² ₋₁₇₂	42 ⁺⁵⁸ ₋₄₂	0.07 ^{+0.07} _{-0.07}	1.10/156
VW Hyi ₂	DN	5.87 ^{+0.41} _{-0.34}	0 ^{+0.01} ₋₀	0.05 ^{+0.06} _{-0.05}	6.66 ^{+0.01} _{-0.01}	49.4 ^{+4.59} _{-4.59}	1214 ⁺⁵⁹ ₋₁₅₃	20 ⁺³⁴ ₋₂₀	0.04 ^{+0.05} _{-0.05}	1.04/114
VW Hyi ₃	DN	6.45 ^{+2.81} _{-1.65}	0 ^{+0.01} ₋₀	0.09 ^{+0.07} _{-0.07}	6.68 ^{+0.01} _{-0.01}	43.1 ^{+3.86} _{-3.86}	948 ⁺¹⁴⁰ ₋₁₁₉	92 ⁺³³ ₋₃₅	0.21 ^{+0.08} _{-0.06}	1.16/131
VW Hyi ₄	DN	4.81 ^{+1.80} _{-1.14}	0 ^{+0.01} ₋₀	0.05 ^{+0.06} _{-0.05}	6.67 ^{+0.01} _{-0.01}	38.5 ^{+4.03} _{-4.02}	870 ⁺³⁴¹ ₋₁₃₄	84 ⁺³³ ₋₄₀	0.19 ^{+0.08} _{-0.08}	1.07/115
VY Aqr	DN	12.0 ⁺¹⁴¹ _{-6.20}	30 ⁺⁶³ ₋₃₀	0.12 ^{+0.27} _{-0.12}	6.66 ^{+0.03} _{-0.03}	5.36 ^{+1.61} _{-1.61}	431 ⁺¹³⁶ ₋₁₂₇	0 ^{+0.01} ₋₀	0.0 ^{+0.01} _{-0.0}	1.05/52
Z Cam	DN	12.5 ^{+2.11} _{-1.43}	54 ⁺⁹ ₋₈	0.23 ^{+0.04} _{-0.04}	6.68 ^{+0.01} _{-0.01}	108.5 ^{+5.13} _{-5.13}	276 ⁺¹³ ₋₁₄	161 ⁺¹² ₋₁₃	0.58 ^{+0.05} _{-0.05}	1.01/1098
GT Mus	AB	5.44 ^{+0.19} _{-0.18}	15 ⁺⁴ ₋₅	0.08 ^{+0.03} _{-0.03}	6.67 ^{+0.01} _{-0.01}	130.4 ^{+4.6} _{-4.7}	259 ⁺⁹ ₋₁₁	18 ⁺⁷ ₋₆	0.10 ^{+0.03} _{-0.03}	1.03/1432
II Peg	AB	3.59 ^{+0.25} _{-0.24}	0 ⁺¹⁵ ₋₀	0.00 ^{+0.08} _{-0.00}	6.67 ^{+0.01} _{-0.01}	23.7 ^{+2.9} _{-2.9}	217 ⁺³⁰ ₋₃₅	0.1 ⁺¹⁹ _{-0.1}	0.01 ^{+0.09} _{-0.01}	1.08/276
σ Gem	AB	2.66 ^{+0.20} _{-0.21}	0 ⁺¹¹ ₋₀	0.0 ^{+0.04} _{-0.0}	6.66 ^{+0.01} _{-0.01}	14.3 ^{+1.36} _{-1.11}	436 ⁺⁴⁵ ₋₄₈	0 ⁺¹⁷ ₋₀	0.0 ^{+0.01} _{-0.0}	0.88/273
UX Ari	AB	2.61 ^{+0.21} _{-0.18}	7 ⁺¹⁵ ₋₇	0.04 ^{+0.11} _{-0.04}	6.67 ^{+0.01} _{-0.01}					

Table 3: Mean values of key parameters for individual classes.

Source Class	T_b	$EW_{6.4}$	$EW_{6.7}$	$EW_{7.0}$	$I_{7.0}/I_{6.7}$
	(keV)	(eV)	(eV)	(eV)	
SSs	27.2 ± 20.8	280 ± 90.0	241 ± 78.3	91 ± 20.1	0.45 ± 0.11
IPs	34.0 ± 4.54	115 ± 9.12	107 ± 16.0	80 ± 6.81	0.71 ± 0.04
Polars	11.4 ± 2.84	66.7 ± 44.4	221 ± 135	74 ± 29.7	0.44 ± 0.14
DNe	10.7 ± 2.04	61.6 ± 18.7	438 ± 84.6	95 ± 18.6	0.27 ± 0.06
ABs	3.6 ± 0.61	$5.50^{+11.1}_{-5.50}$	286 ± 58.5	12.1 ± 7.36	0.08 ± 0.04
GRXE	$15.1^{+0.4}_{-0.7}/6.64^{+0.40}_{-0.42}$	110^{+9}_{-10}	490 ± 15	110 ± 10	0.2 ± 0.08

Note: The errors of the means are at the $1\text{-}\sigma$ level. The GRXE values are from Uchiyama et al. (2013) and Yuasa et al. (2012) are included for comparison. T_b of GRXE: 6.64 keV from Uchiyama et al. (2013) of 2-10 keV range fitting; 15 keV from Yuasa et al. (2012) of 2-50 keV range fitting. See Discussion for details.

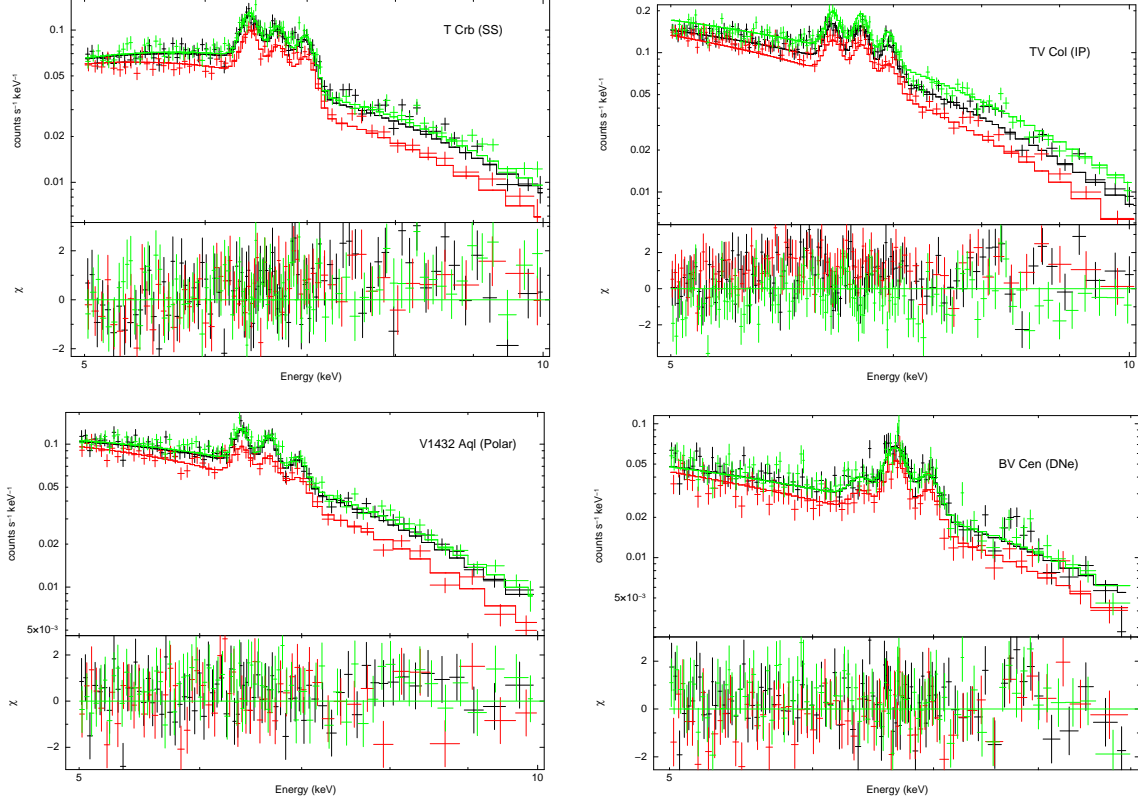


Fig. 2.— Examples of CV spectra with the best-fit model of an absorbed apec (with the metallicity set to zero) plus three Gaussians for the Fe lines. The black-, red- and green-colored data points represent spectra from XIS-0, -1, and -3 chips. Upper left - T Crb (SS); upper right - TV Col (IP); lower left - V1432 Aql (polar); lower right - BV Cen (DNe). Spectra are rebinned for plotting only.

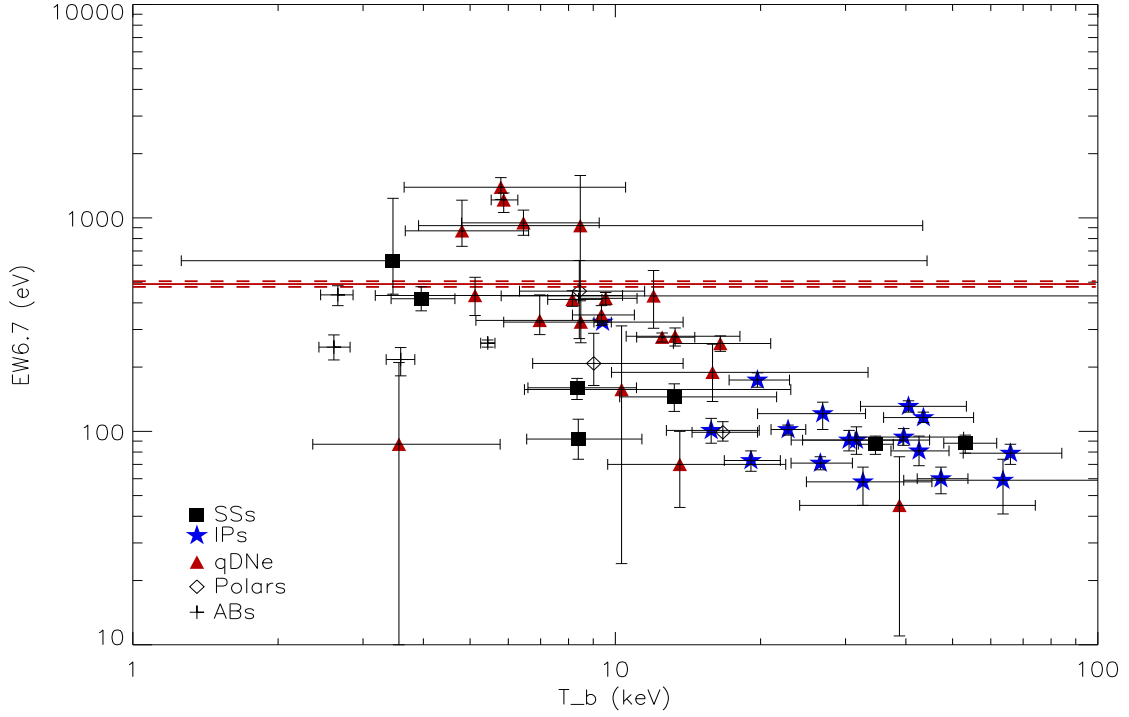


Fig. 3.— $EW_{6.7}$ vs. T_b of our sample sources. Individual classes are labeled differently. The solid and dashed red lines mark the $EW_{6.7}$ value and its 1σ error range of the GRXE. Fig 3 to Fig 7 includes multiple measurements for sources with multiple observations (see Table 2 for details): SS73-17 (two measurements), XY Ari (two measurements), VW Hyi (four measurements).

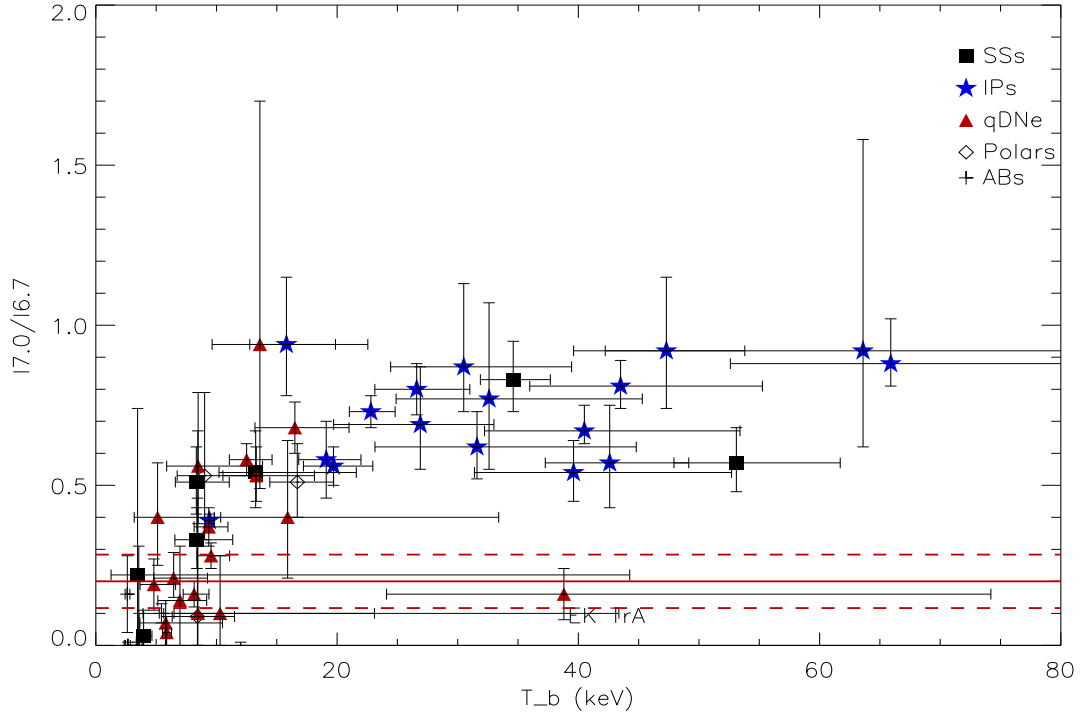


Fig. 4.— $I_{7.0}/I_{6.7}$ vs. T_b of our sample sources. The solid and dashed red lines mark the $I_{7.0}/I_{6.7}$ value and 1σ error range of the GRXE. The labeled abnormal DN, EK TrA, is discussed in the text.

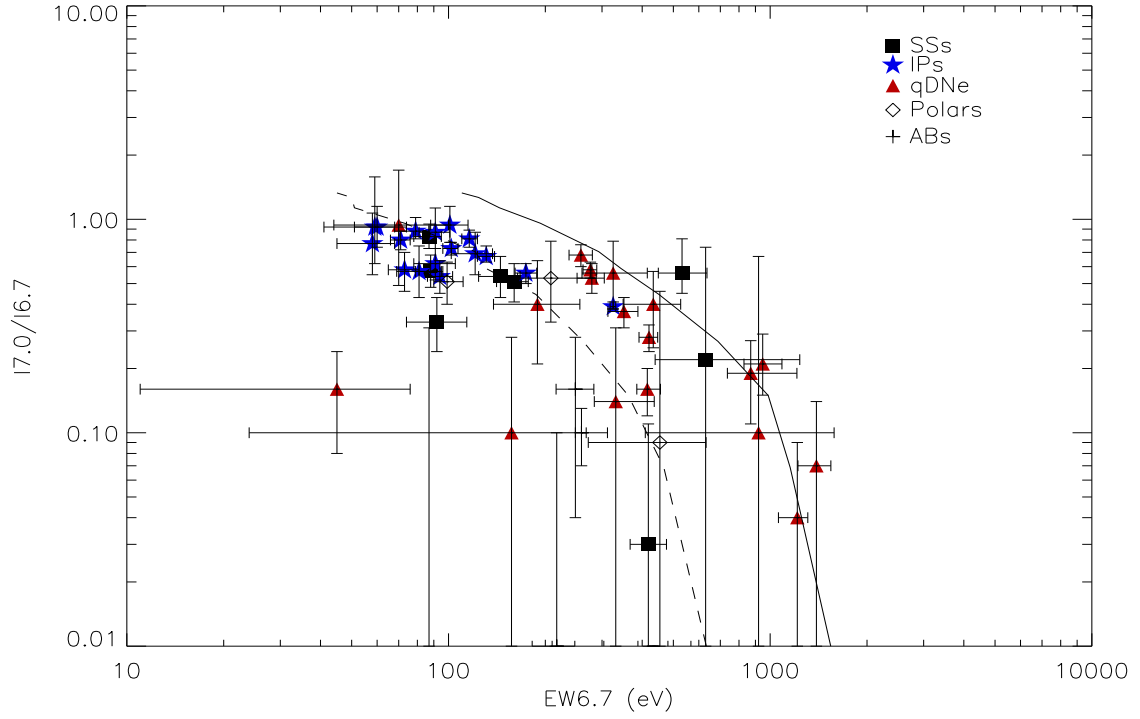


Fig. 5.— $I_{7.0}/I_{6.7}$ vs. $EW_{6.7}$ of our sample sources, compared with the values predicted by cooling flow model with metallicity $Z = Z_{\odot}$ (solid line) and $Z = 0.3Z_{\odot}$ (dashed line), respectively.

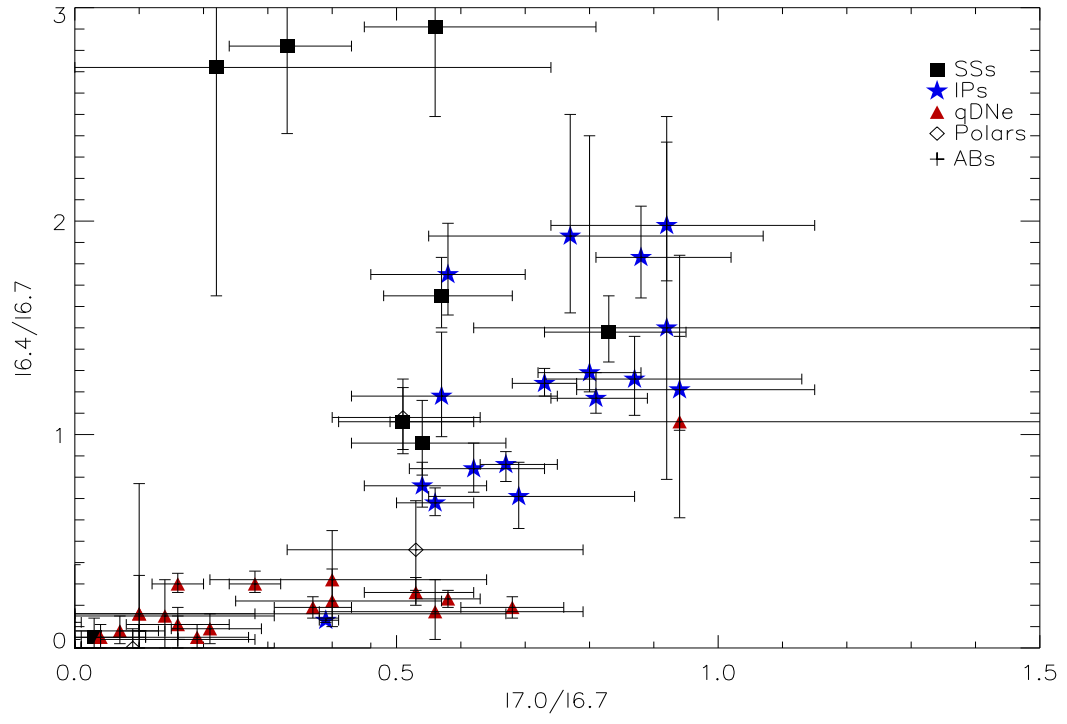


Fig. 6.— $I_{6.4}/I_{6.7}$ vs. $I_{7.0}/I_{6.7}$ of our sample sources.

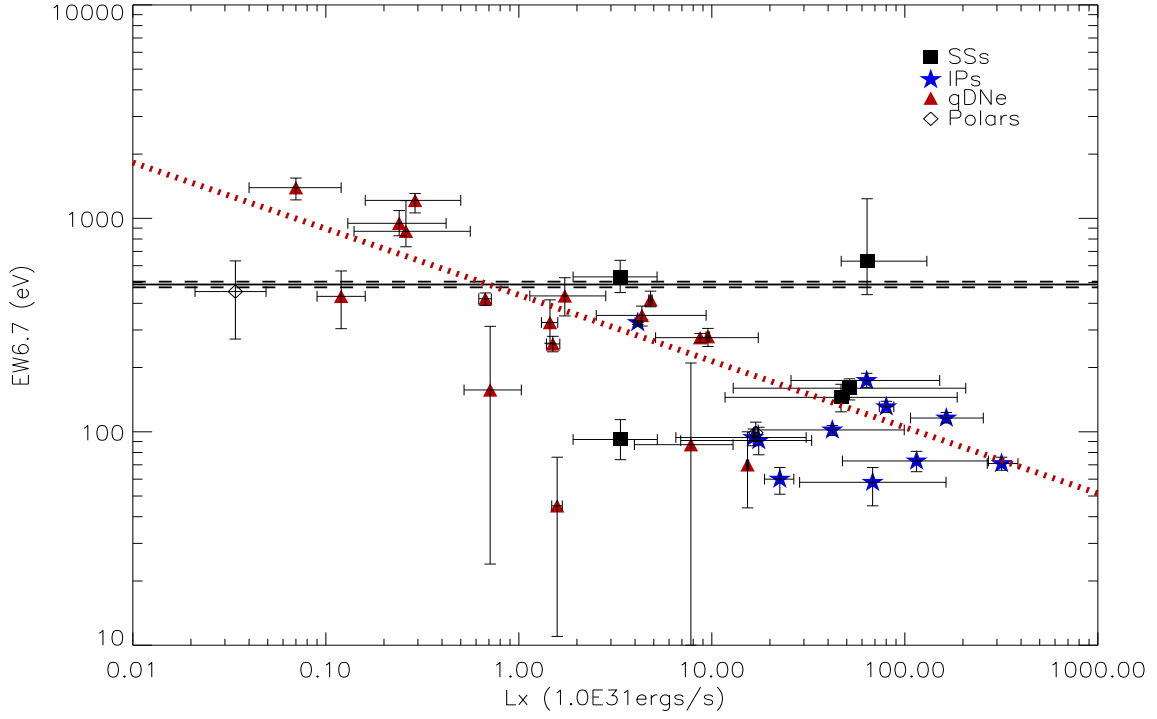


Fig. 7.— $EW_{6.7}$ vs. $L_{2-10\text{keV}}$ of our sample CVs. The solid and dashed black lines mark the $EW_{6.7}$ value and error range of the GRXE. The red dotted line represents the best-fitted log-log linear relation for DNe only (see the text for details).

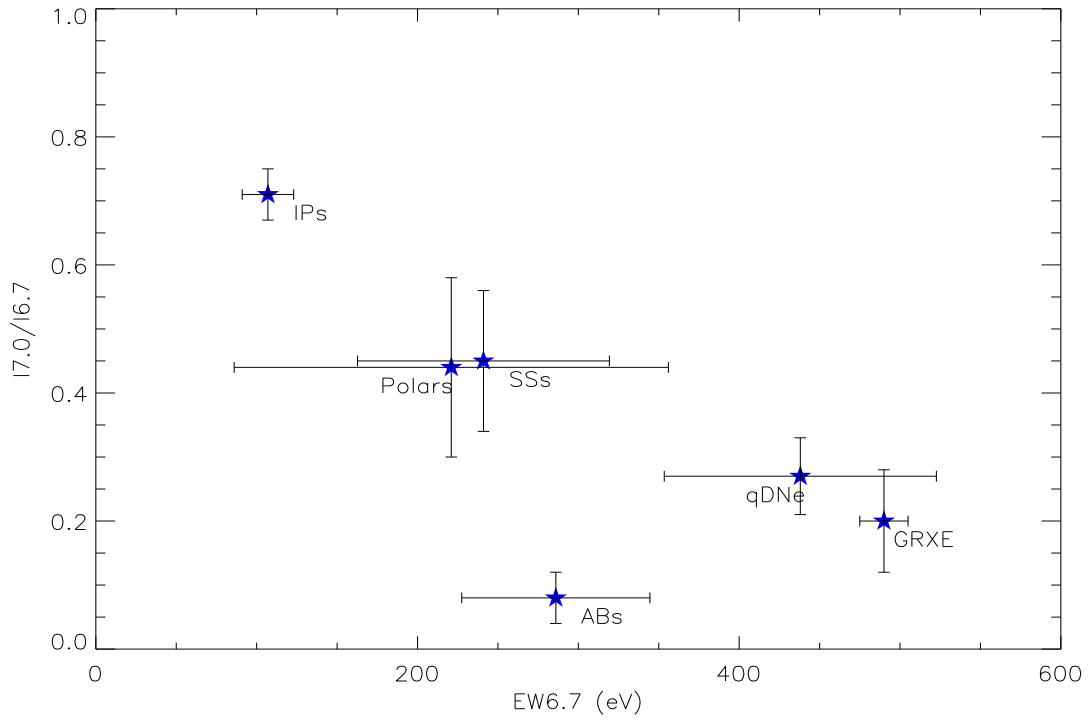


Fig. 8.— Mean $I_{7.0}/I_{6.7}$ vs. mean $EW_{6.7}$ of our sample classes, compared with the values of the GRXE.

REFERENCES

- Anzolin, G., de Martino, D., Falanga, M., et al., 2009, *A&A*, 501, 1047
- Arnaud K., 1996, in Jacoby G. H., Barnes J., eds, *ASP Conf. Ser. Vol. 101, Astronomical Data Analysis Software and Systems V*. Astron. Soc. Pac., San Francisco, p. 17
- Barlow, E. J., Knigge, C., Bird, A.J., et al., 2006, *MNRAS*, 372, 224
- Barry, R. K., Mukai, K., Sokoloski, J.L., et al., 2008, *ASPC*, 401, 52
- Baskill, D. S., Wheatley, P. J., & Osborne, J. P., 2005, *MNRAS*, 357, 626
- Berdyugina, S.V., Jankov, S., Ilyin, I., et al., 1998, *A&A*, 334, 863
- Byckling, K., Mukai, K., Thorstensen, J. R., & Osborne, J. P., 2010, *MNRAS*, 408, 2298
- de Martino D., Bonnet-Bidaud, J.-M., Mouchet, M., et al., 2006, *A&A*, 449, 1151
- Ebisawa, K., Yamauchi, S., Tanaka, Y., et al., 2008, *PASJ*, 60, S223
- Eker, Z., Ak, N. F., Bilir, S., et al., 2008, *MNRAS*, 389, 1722
- Eze, R.N.C., *New Astronomy*, 36, 64
- Ezuka, H., & Ishida, M., 1999, *ApJS*, 120, 277
- Franciosini, E., Pallavicini, R., & Tagliaferri, G., 2001, *A&A*, 375, 196
- Gansicke, B., Beuermann, K., & de Martino, D., 1995, *A&A*, 303, 127
- Gansicke, B., Beuermann, K., & Thomas, H., 1997, *MNRAS*, 289, 388
- Gansicke B.T., Dillon, M., Southworth, J., et al., 2009, *MNRAS*, 397, 2170
- Godon, P., Sion, E. M., Levay, K., et al., 2012, *ApJS*, 203, 29

- Gray, D., 2008, *The Observation and Analysis of Stellar Photospheres*, Cambridge University Press, 3rd edition
- Hayashi, T., Ishida, M., Terada, Y., et al., 2011, *PASJ*, 63, 739
- Hellier, C., Mukai, K., 2004, *MNRAS*, 352, 1037
- Hong, J., van den Berg, M., Grindlay, J. E., et al., 2012, *ApJ*, 746, 165
- Ikis Gun, G., Karagul, A., & Gok, F., 2013, *New Astronomy*, 25, 1
- Ishida, M., & Ezuk, H., 1999, *ASPC*, 157, 333
- Ishida, M., Okada, S., Hayashi, T., et al., 2009, *PASJ*, 61, 77
- Kepler, S. O., Kleinman, S.J., Nitta, A., et al., 2007, *MNRAS*, 375, 1315
- Kepler, S. O., Pelisoli, I., Jordan, S., et al., 2013, *MNRAS*, 429, 2934
- Li, Z., & Wang, D., 2007, *ApJ*, 668, 39
- Longair, M. S., 2011, *High Energy Astrophysics*, Cambridge University Press, 3rd edition
- Li, J.-T., & Wang, Q. D. 2013, *MNRAS*, 428, 2085
- Mallik, S. V., 1998, *A&A*, 338, 623
- Molaro, M., Khatri, R., & Sunyaev, R. A. 2014, *A&A*, 564, 107
- Mukai, K., Zietsman, E., & Still, M., 2009, *ApJ*, 707, 652
- Mukai, K., et al., 2012, *Baltic Astronomy*, 21, 54
- Muno, M. P., Baganoff, F. K., Brandt, W. N., Park, S., & Morris, M. R., 2007, *ApJ*, 656, 69
- Neustroev, V., & Zharikov, S., 2008, *MNRAS*, 386, 1366

- Neustroev, V., & Tsygankov, S., 2014, *The X-ray Universe*, 294
- Ozdonmez, A., Ak, T., & Bilir, S., 2015, *New Astronomy*, 34, 2340
- Perez, K., Hailey, C.J., Bauer, F.E., et al. 2015, *Nature*, 520, 646
- Perryman, M.A.C., lindegren, L., Kovalevsky, J., et al., 1997, *A&A*, 323, L49
- Pretorius, M. L., & Knigge, C., 2012, *MNRAS*, 419, 1442
- Pretorius, M., & Mukai, K., 2014, *MNRAS*, 442, 2580
- Rana, R., Singh, K. P., Schlegel, E. M., & Barrett, P. E., 2006, *ApJ*, 642, 1042
- Reis R. C., Wheatley, P.J., Gansicke, B.T., et al., 2013, *MNRAS*, 430, 1994
- Revnivtsev, M., Sazonov, S., Gilfanov, M., Churazov, E., & Sunyaev, R., 2006, *A&A*, 452, 169
- Revnivtsev, M., Sazonov, S., Churazov, E., et al., 2009, *Nature*, 458, 1142
- Revnivtsev, M. G., Filippova, E. V., & Suleimanov, V. F., 2014, *Astronomy Letters*, V40., No. 4, 177
- Ritter, H., & Kolb, U., 2003, *A&A*, 404, 301
- Saitou, K., Tsujimoto, M.m Ebisawa, K., et al., 2012, *PASJ*, 64, 88
- Sazonov, S., revnivtsev, M., Gilfanov, M., et al., 2006, *A&A*, 450, 117
- Schlegel, E.M., Shipley, H.V., Rana, V.R., et al., 2014, *ApJ*, 797, 38
- Terada, Y., 2010, *ApJ*, 721, 1908
- Thorstensen, J., 2003, *ApJ*, 126, 3017

- Thorstensen, J. R., Lpine, S., & Shara, M., 2008, *AJ*, 136, 2107
- Uchiyama, H., Nobukawa, M., Tsuru, T. G., Koyama, K., & Matsumoto, H. 2011, *PASJ*, 63, 903
- Uchiyama, H., Nobukawa, M., Tsuru, T., et al., 2013, *PASJ*, 65, 19
- Warwick, R. S., Byckling, K., & Prez-Ramrez, D., 2014, *MNRAS*, 438, 2967
- Watson, M. G., 1995, *MNRAS*, 273, 681
- Wijnen, T. P. G., Zorotovic, M., & Schreiber, M. R., 2015, *A&A*, 577, 143
- Worrall, D. M., Marshall, F. E., Boldt, E. A., & Swank, J. H. 1982, *ApJ*, 255, 111
- Yamauchi, S., Ebisawa, K., Tanaka, Y., et al., 2009, *PASJ*, 61, S225
- Yuasa, T., Nakazawa, K., Makishima, K., et al., 2010, *A&A*, 520, 25
- Yuasa, T., Makishima, K., & Nakazawa, K., 2012, *ApJ*, 753, 129
- Zorotovic M., Schreiber M. R., & Gansicke B. T., 2011, *A&A*, 536, 42